ACS APPLIED NANO MATERIALS

www.acsanm.org

Article

Hydrothermal Synthesis of Ni_3TeO_6 and Cu_3TeO_6 Nanostructures for Magnetic and Photoconductivity Applications

Javier Fernández-Catalá,* Harishchandra Singh,* Shubo Wang, Hannu Huhtinen, Petriina Paturi, Yang Bai, and Wei Cao

Cite This: *ACS Appl. Nano Mater.* 2023, 6, 4887−4897

Read Online

ACCESS | Metrics & More | Article Recommendations | Supporting Information

ABSTRACT: Despite great attention toward transition metal tellurates especially M_3TeO_6 (M = transition metal) in magnetoelectric applications, control on single phasic morphology-oriented growth of these tellurates at the nanoscale is still missing. Herein, a hydrothermal synthesis is performed to synthesize single-phased nanocrystals of two metal tellurates, i.e., Ni_3TeO_6 (NTO with average particle size ∼37 nm) and Cu_3TeO_6 (CTO ∼ 140 nm), using NaOH as an additive. This method favors the synthesis of pure NTO and CTO nanoparticles without the incorporation of Na at pH = 7 in MTO crystal structures such as $Na_2M_2TeO_6$, as it happens in conventional synthesis approaches such as solid-state reaction and/or coprecipitation. Systematic characterization techniques utilizing in-house and synchrotron-based characterization methods for the morphological, structural, electronic, magnetic, and photoconductivity properties of nanomaterials showed the absence of Na in individual particulate single-phase MTO nanocrystals. Prepared MTO nanocrystals also exhibit slightly higher antiferromagnetic interactions (e.g., T_N-NTO = 57 K and T_N-CTO = 68 K) compared to previously reported MTO single crystals. Interestingly, NTO and CTO show not only a semiconducting nature but also photoconductivity. The proposed design scheme opens the door to any metal tellurates for controllable synthesis toward different applications. Moreover, the photoconductivity results of MTO nanomaterials prepared serve as a preliminary proof of concept for potential application as photodetectors.

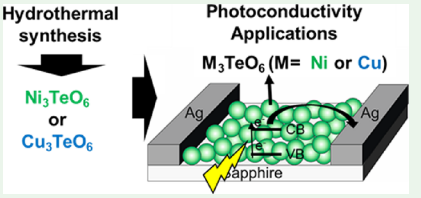

KEYWORDS: *transition metal tellurates, hydrothermal synthesis, optical properties, photoconductivity, magnetism*

INTRODUCTION

Transition metal tellurates in particular M_3TeO_6 (MTO; M = Ni, Co, Mn, Cu) exhibit a broad variety of technologically important properties. Most of reported results focus on antiferromagnetic ordering at low temperatures combined with magnetoelectric properties.[1−3] They are primarily classified as type II multiferroics and have recently gained great importance.[2,4−6] For instance, the longest known tellurate of this family is Ni_3TeO_6 (NTO), which was structurally investigated in the year 1967.[7] NTO crystallizes in corundum (Al_2O_3 type) structures with a polar R3 space group geometry. Ni cations in NTO reside in three different crystallographic sites and form face-shared, edge-shared, and corner-shared distorted NiO_6 octahedra. TeO_6 also forms a distorted octahedron. While the magnetic property of NTO at room temperature does not seem interesting, the low-temperature characteristic of NTO is intriguing and has drawn tremendous interest due to its unusual spin-flop transition, a complex magnetic field temperature phase diagram, and the largest magnetoelectric coupling.[8] Recently, spin-driven pyroelectricity (colossal magnetoelectric effect) below the antiferromagnetic (AFM) ordering temperature of T_N = 52 K was reported for NTO, together with an exceptional possibility of a magnetoelectric switching without hysteresis.[1,2,4] A few more reports summarize that already small changes in electric and magnetic fields are sufficient for a spin-flop transition in NTO particles.[8−10] Furthermore, Cu_3TeO_6 (CTO) crystallizes in the cubic system of space group Ia-3 and exhibits an interesting structural feature. Each TeO_6 octahedron connects to 12 distorted CuO_6 octahedra, forming a unique three-dimensional framework. Three notable spin lattices, namely, equilateral triangle, isosceles triangle, and planar hexagon, are built by CuO_6 octahedra via corner-sharing or edge-sharing. Concerning the low-temperature AFM property, CTO adopts a bixbyite-type crystal structure and orders in a "three-dimensional spin web" with hexagonal arrangements of the magnetic moments below T_N = 63 K.[3,11,12] Besides these reports, which mainly focus on magnetoelectric application, an additional report also explores the photocatalytic activity[13] and electrochemical properties[14] of NTO and their application as sensor of CTO,[15] indicating a possible bigger picture of MTO with nanoscale features.

Received: February 10, 2023
Accepted: February 27, 2023
Published: March 9, 2023

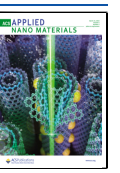

Scheme 1. Hydrothermal Synthetic Procedure Followed for the Preparation of Single-Phase Ni_3TeO_6 and Cu_3TeO_6 Nanostructures

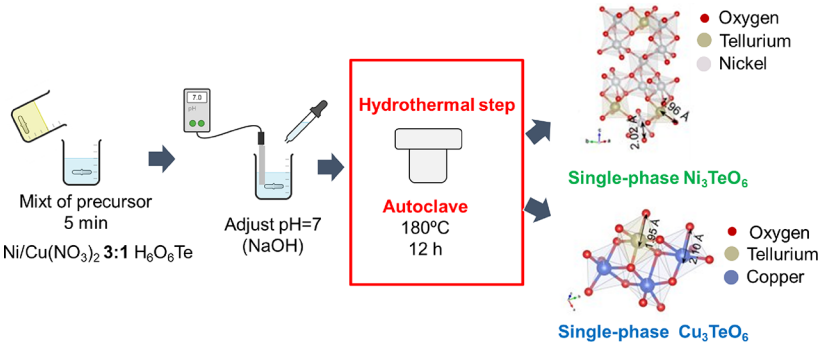

While the role of transition metals in several transition metal-based complexes including MTO has been already been studied,[16] the role of tellurium (Te) in such compounds is still a paradox. Te, a chalcogenide high-Z element, has already provided great development potential in the fields of high-performance photodetectors, field effect transistors, and thermoelectric devices in recent years.[17,18] However, the similar device potential for transition metal-based tellurium oxide is still critical.[15] Te-based compounds, in particular a combination of transition metals, Te, and oxygen (referred to here as tellurate, i.e., MTO), have recently been reported to be a growing material class owing to the higher electronic conductivity of Te. It has recently been seen to concur with the electronic conductivity issue in transition metal-based complexes when combined with Te toward wider energy applications;[19,20] however, it is rarely engineered and implemented for morphology-dependent low-dimensional nanostructures for photonics, optoelectronics, and/or catalytic applications. Most of the research on such combination, for example MTO, has been dedicated to the condensed matter physics side such as magnetic properties due to the presence of magnetic elements (M = Ni, Co, Mn, Cu in MTO, all having responsible free electrons in their d orbital). However, the intrinsic features of Te, mainly higher electronic conductivity and its chalcogen nature, have been overlooked. Inclusion of these characteristics of M and Te in MTO might result in additional applications aforesaid above and is explored in this work.

Previously, MTO such as NTO and CTO has been grown mostly using conventional synthesis approaches such as solid-state reaction and/or coprecipitation methods.[2,21,22] These processes show challenges in getting single-phase MTO materials probably because of the structural diversity of Te-based compounds and a wide range of possible Te−O bond lengths and in the size of the particles due to the high temperatures used.[23,24] Aforesaid potential applications and reported complicated synthesis demand a cost-effective and facile approach for MTO with improved performances and are the focus of the present work. Alternative synthesis of MTO materials can be found in wet chemical methodologies (sol−gel or co-precipitation) to enable the materials' applications in photocatalysis,[13] electrocatalysis,[25] and sensors.[15] Indeed, the hydrothermal approach benefits wet synthetic routes and is widely used in ceramics synthesis.[26,27] This methodology presents several advantages, i.e., excellent control of the composition and the size distribution at the nanoscale, compared to solid-state synthetic methodologies.[28] This composition control is an important parameter in the synthetic procedures of novel ceramic materials,[29−31] such as MTOs, since the incorporation of additives, such as NaOH, to control the pH and the crystal growth mechanism can produce different phases in the final product, such as $Na_2M_2TeO_6$ (M = Ni or Cu).[32,33] Consequently, the design of novel synthetic strategies of MTOs, with optical, photoconductivity, and magnetic properties using additives (NaOH) and novel procedures (hydrothermal synthesis), is crucial to opening the door to this family of metal tellurates for different applications. Nevertheless, it is admitted that the insufficient reserve of Te on the earth may be a drawback for the application of the materials studied in this work.[34,35] It is thus important to consider the abundancy of the precursors in future works.

With this in mind, in this work two metal tellurates based on Ni (NTO) and Cu (CTO) have been synthesized using the hydrothermal method by adding NaOH to control the pH and increase the growth speed of MTO crystals. The materials synthesized have been systematically characterized by utilizing in-house and synchrotron-based characterization methods for their morphological, structural, electronic, magnetic, and photocatalytic properties. The NTO and CTO synthesized using hydrothermal methodology presented optical, photoconductivity, and magnetic properties. The measured current−voltage response in the dark and under illumination with different wavelengths serves as a proof of concept for potential applications in photodetection. The magnetic transition at low temperatures demonstrates a potential application as a thermal-magnetic sensor. Moreover, the synthetic methodology used for MTO may also be transferred to their chalcogen analogues (Se, P, and S), which broadens the applicability.

EXPERIMENTAL SECTION

Materials. Copper nitrate ($Cu(NO_3)_2{\cdot}3H_2O$, 99−104%, Sigma-Aldrich), nickel nitrate ($Ni(NO_3)_2{\cdot}6H_2O$, 98%, Alfa Aesar), telluric acid (H_6O_6Te, 98%, Sigma-Aldrich), sodium hydroxide (NaOH, 97%, Sigma-Aldrich), absolute ethanol (EtOH, 99.5%, ETAX), and deionized water were used in the present work. All reactants were used as received, without any further purification.

Materials Preparation. Ni_3TeO_6 and Cu_3TeO_6 materials were prepared by hydrothermal synthesis. For the synthesis of Ni_3TeO_6 and Cu_3TeO_6, using hydrothermal synthesis and NaOH as an additive (see Scheme 1), appropriate amounts of reagents, $Ni(NO_3)_2{\cdot}6H_2O$ or $Cu(NO_3)_2{\cdot}3H_2O$, and H_6O_6Te, were mixed in a stoichiometric ratio (3:1, respectively) in deionized (DI) water (60 mL). This solution was stirred vigorously for 10 min. Then, NaOH (2 M) solution was used to adjust the pH to 7 in vigorous stirring. The mixture adjusted to pH = 7 was stirred for 5 min. This solution was transferred to an

https://doi.org/10.1021/acsanm.3c00630
ACS Appl. Nano Mater. 2023, 6, 4887−4897

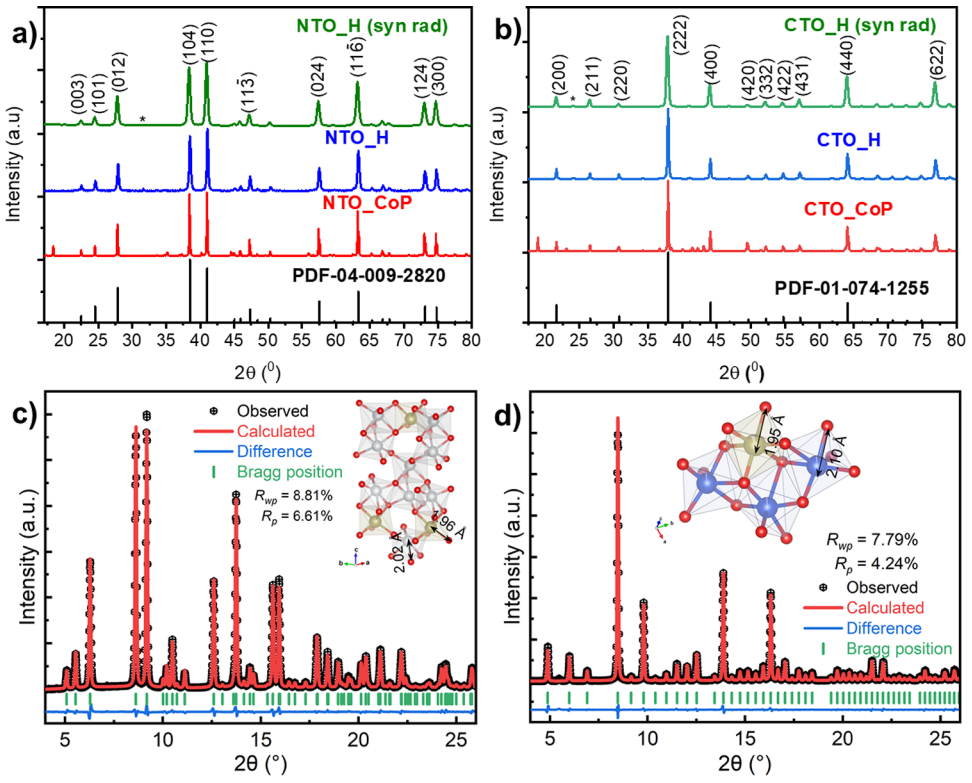

Figure 1. PXRD patterns for synthesized NTO and CTO samples: (a) NTO samples and (b) CTO samples. Rietveld refinement results for SXRD profiles and polyhedral view from fitted data of (c) NTO_H and (d) CTO_H.

autoclave (100 mL) and heated up to 180 °C for 12 h. The mixtures were centrifuged (5000 rpm) to collect the solid materials, and they were washed three times with DI water and three times more with EtOH in order to clean the samples from some impurities obtained during the synthetic process. The solid obtained was calcined at 600 °C for 2 h. The as-obtained Ni_3TeO_6 and Cu_3TeO_6 powders are named as NTO_H, and CTO_H, respectively.

For comparison, Ni_3TeO_6 and Cu_3TeO_6 materials were prepared using the co-precipitation method. For the latter approach, appropriate amounts of reagents $Ni(NO_3)_2{\cdot}6H_2O$ or $Cu(NO_3)_2{\cdot}3H_2O$ and H_6O_6Te were mixed in a stoichiometric ratio in DI water (60 mL). This solution was stirred vigorously for 10 min. Then, NaOH (2 M) solution was used to adjust the pH to 7. The mixture was stirred for 8 h at 80 °C on a hot plate. The mixtures were centrifuged (5000 rpm) to collect the solid materials, and they were washed three times with DI water and three times more with EtOH in order to clean the samples of some impurities obtained during the synthetic process. The solid obtained was calcined at 600 °C for 2 h. Ni_3TeO_6 and Cu_3TeO_6 obtained by co-precipitation synthesis are named as NTO_CP and CTO_CP, respectively.

Materials Characterization. Powder XRD patterns at room temperature were performed with Rigaku SmartLab 9 kW equipped with a five-axis θ–θ goniometer and a 1D solid-state detector and scintillator using Co Kα (λ = 1.79 Å, 40 kV, 135 mA) radiation. To obtain microstructures of the bulk, synchrotron X-ray diffraction (SXRD) measurements were carried out at the Brockhouse High Energy Wiggler Beamline (Canadian Light Source (CLS), Canada).[36] The data acquisition was performed in transmission mode, so a 2D Perkin Elmer detector, 200 × 200 μm^2 in pixel size and 40 × 40 cm^2 in area, was placed downstream of the powders in a Kapton capillary. A monochromatic focused beam of 30 keV was used to obtain the patterns. Different from in-house powder XRD, SXRD owns larger penetration depths, thus probing the microstructures of the whole particles. The calibrated X-ray wavelength and sample-to-detector distance from a Ni calibrant were λ = 0.4087 Å and 478.8 mm, respectively. A total of 64 snapshots were acquired, and an exposure time of 0.2 s was used to ensure a good data statistic. The obtained raw 2D diffraction patterns were integrated in the radial direction by GSAS-II software;[37] the resulting 1D SXRD profiles were analyzed using Rietveld refinement analysis.[38] Transmission electron microscopy (TEM) coupled with electron energy loss spectroscopy (EELS) and energy-dispersive spectroscopy (EDS) mapping was carried out using JEOL JEM-2200FS EFTEM/STEM. Field emission scanning electron microscope (FESEM) images were taken using Zeiss Ultra Plus FESEM. The specific surface areas, average pore sizes, and volumes of the synthesized materials were measured with N_2 adsorption at −195 °C using a micrometrics ASAP 2020 surface analyzer. Before the analyses, the samples were evacuated for 4 h at 250 °C. Optical spectroscopies were obtained using a Shimadzu UV-2600 spectrophotometer. XPS measurements were performed with Al Kα using Thermo Fisher Scientific ESCALAB 250Xi XPS System. Energy calibration of the XPS was performed by using the C 1s peak at 284.8 eV.

Magnetic Property Measurements. The temperature dependence of the zero-field-cooled (ZFC) and field-cooled (FC) magnetization was measured for the powder samples between the temperatures of 5 and 300 K with a Quantum Design MPMS XL SQUID magnetometer with the external magnetic field of B = 10 mT, 100 mT, and 5 T. The magnetic hysteresis curves were recorded in magnetic fields up to 5 T at temperatures of 5 and 300 K.

Device Fabrication and Photoconductivity Measurements. To assess the feasibility of being used in photodetectors, the synthesized NTO and CTO were made into a conventional, transverse sensor configuration. The NTO and CTO nano-powders were deposited on sapphire substrates. The methodology used was drop coating using dispersion of NTO or CTO (50 mg) in EtOH (5 mL). The drops deposited on sapphire substrates were dried at 80 °C. Ag electrodes were then coated on the sample surfaces to form in-plane electrode configurations with approximately 700 μm gaps. The size of the lab device was 1 × 1 cm. Current–voltage (I–V) curves were obtained using the 2450 SourceMeter (Keithley, USA) in the dark and under different incident photon energies, i.e., 1.88, 2.25, and 3.06 eV. Monochromatic lasers (OBIS LX/LS series, Coherent, USA) with wavelengths of 660, 552, and 405 nm, respectively, were used as

https://doi.org/10.1021/acsanm.3c00630
ACS Appl. Nano Mater. 2023, 6, 4887–4897

the light sources. The power density of the incident lights was about 4 W/cm^2. Sheet resistance was calculated from the $I-V$ curves.

RESULTS AND DISCUSSION

Crystal, Morphological, and Electronic Structures. To study the crystal structure of the metal tellurates (NTO and CTO) synthesized by hydrothermal synthesis, the final powders of the synthesis were characterized by lab-source XRD analysis (Figure 1). Sample NTO_H shows characteristic diffraction peaks at 2θ = 22.50, 24.55, 27.84, 38.487, 41.04, 47.31, 57.52, 63.27, 73.07, and 74.78°, which correspond to the characteristic peaks of (003), (101), (012), (104), (110), (11$\bar{3}$), (024), (11$\bar{6}$), (124), and (300) lattice planes of Ni_3TeO_6 (PDF 04-009-2820) (see Figure 1a). This comparative XRD result indicates that the phased NTO is synthesized without incorporation of Na in the crystalline structure of metal tellurate. However, the NTO_H diffraction patterns (Figure 1a) present a small broad peak at 31.08°, indicating possible impurities of another metal tellurate, $NiTe_2O_5$ (PDF 00-027-1306). With the aim of deeply studying the crystalline structure of NTO, the sample was analyzed by synchrotron radiation XRD and converted to the same 2θ angle scale as lab-source X-ray (Figure 1a).[24,39] Under synchrotron radiation, XRD NTO_H shows mainly characteristic diffraction peaks of Ni_3TeO_6 (PDF 04-009-2820), indicating that this is the main phase. However, a small peak at 31.62° is observed indicating the presence of a $NiTe_2O_5$ impurity. The appearance of $NiTe_2O_5$ in low amount can be ascribed to the calcination step, taking into account that this phase can be generated by the Ni_3TeO_6 decomposition at high temperature.[25,40] This fact highlights the relevance of using synchrotron radiation XRD to characterize the crystalline structure of inorganic materials.[41] The CTO_H samples (Figure 1b) show characteristic diffraction peaks at 2θ = 20.93, 25.90, 30.10, 37, 25, 43.42, 54.07, 56.52, 63.48, 70.05, and 76.377°, which correspond to the characteristic peaks of (200), (211), (220), (222), (400), (422), (431), (440), (600), and (622) lattice planes of Cu_3TeO_6 (PDF 01-074-1255), respectively, related to the Cu_3TeO_6 crystalline single phase. The CTO_H sample was analyzed by synchrotron radiation XRD to confirm that CTO_H presents a single phase (Cu_3TeO_6). CTO_H under synchrotron radiation XRD (Figure 1b) shows only characteristic diffraction peaks of Cu_3TeO_6 (PDF 01-074-1255). This XRD result indicates that the single-phase CTO is synthesized without incorporation of Na in the crystalline structure of the metal tellurate. In this work, the effect of changing the stoichiometric ratio (2:1 from 3:1) in the synthesis of materials by the hydrothermal method was also studied. The XRD analysis of NTO samples (2:1 and 3:1) (Figure S1a) shows that a change of stoichiometric ratio generated multiphase materials. However, in CTO samples after changing the stoichiometric ratio (2:1 from 3:1), we obtain single-phase Cu_3TeO_6, indicating the relevance of the transition metal used. The results obtained by XRD analysis show that the stoichiometric ratio of $Ni(NO_3)_2{\cdot}6H_2O$ or $Cu(NO_3)_2{\cdot}3H_2O$ with H_6O_6Te is a key factor to obtain single-phase M_3TeO_6 (M = Ni or Cu).

To compare the hydrothermal methodology with co-precipitation methodology, the metal tellurates were synthesized by co-precipitation (NTO_CP and CTO_CP) methodology and they were analyzed by lab-source XRD (Figure 1a,b). The NTO_CP sample (Figure 1a) presents mainly the characteristic peaks of the phase Ni_3TeO_6. However, in this methodology is also observed a peak at 2θ = 18.46°, indicating that Na has been incorporated in the crystalline structure of Ni_3TeO_6 forming the crystal phase $Na_2Ni_2TeO_6$ (PDF 00-058-0052), as it was observed previously in the literature for materials synthesized by solid-state methodology.[42,43] This effect is also observed in CTO_CP (see Figure 1b), where the material, prepared by coprecipitation, shows the characteristic peak (2θ = 18.94°) of the crystalline metal tellurate $Na_2Cu_2TeO_6$[42] (PDF 04-011-7562). This evidence makes clear that the co-precipitation approach at pH = 7 using NaOH favors the incorporation of Na in the crystal structure of the metal tellurates forming multiphase compounds. Therefore, the hydrothermal synthesis benefits the pure metal tellurates using NaOH as an additive compared to other conventional methods, e.g., co-precipitation synthesis. The pristine metal tellurates synthesized using NaOH by hydrothermal synthesis might be achieved due to the benefits of using hydrothermal synthesis.[44] The high pressure and temperature generated in the hydrothermal method than the co-precipitation method might change the nucleation, self-assembly, and growth of the crystals, obtaining new and more crystalline phases and different morphologies, as was previously reported in ceramic synthesis.[45,46] In the hydrothermal methodology performed in this work, the solution with precursors was incorporated in the autoclave after only 5 min of addition of NaOH. Then, the contact with Na^+ and another cation (Te^{6+} and Ni^{2+}) is low before the ions started the nucleation to perform the self-assembly and crystal growth due to the high temperature and pressure inside of the autoclave that favor the nucleation kinetic.[44] However, the co-precipitation method was performed for 8 h at 80 °C at ambient pressure in stirring; this process helps to hold the required cations close together in the reaction medium, letting the contact and the coordination between the different ions,[47] including Na^+. Then, Na^+ might be incorporated in the structure of the final product more easily than in the hydrothermal method.

To clarify the crystal structures of hydrothermally synthesized NTO and CTO, Rietveld refinements were conducted on the SXRD profiles (see Figure 1c,d). Results show a good fit to a rhombohedral (space group: $R3$) Ni_3TeO_6 with lattice constants $a = b$ = 5.109 Å and c = 13.7549 Å and a cubic (space group: $Ia\text{-}3$) Cu_3TeO_6 with lattice constants $a = b = c$ = 9.5350 Å. Tables S.1 and S.2 summarize the refined unit cell structural parameters and occupation of atoms, respectively.

The morphology of the metal tellurates prepared in this work by hydrothermal synthesis (NTO_H and CTO_H) was studied by TEM and SEM analyses. TEM analysis (Figure 2a,b) reveals that the metal tellurate materials based on Ni and Cu are present in the form of nanoparticles (NPs) or particles. NTO_H has a heterogeneous morphology based on NPs, as shown in Figure 2a, with an average size of 37 nm (Figure S.2a). The CTO_H sample also presents a varied morphology (Figure 2b), although a cubic NP predominates with an average size of 140 nm (see Figure S.3b). SEM images of NTO_H (Figure S3a) also disclose the presence of NPs. CTO_H presents a heterogeneous morphology as the NTO_H sample; nevertheless, the size of the CTO_H particles (Figure S2b) is bigger than that of the NTO_H sample, confirming the observation obtained by TEM. HR-TEM images (Figure 2c,d) show the high crystallinity of the metal tellurates. NTO_H (Figure 2c) presents a d spacing of ~2.23 Å corresponding to the (11$\bar{3}$) plane for Ni_3TO_6 (PDF

https://doi.org/10.1021/acsanm.3c00630
ACS Appl. Nano Mater. 2023, 6, 4887−4897

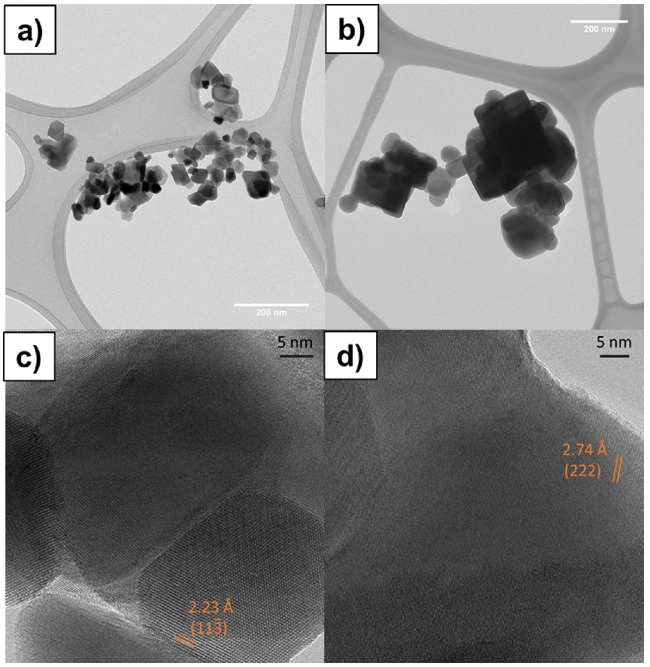

Figure 2. Transmission electron microscopy images for synthesized NTO_H and CTO_H samples; (a) NTO_H samples at low resolution (scale bar: 200 nm), (b) CTO_H samples at low resolution (scale bar: 200 nm), (c) NTO_H samples at high resolution (scale bar: 5 nm), and (d) CTO_H samples at high resolution (scale bar: 5 nm).

04-009-2820), and a d spacing of ~2.74 Å is detected for CTO_H (Figure 2d), corresponding to the (222) plane for Cu_3TeO_6 (PDF 01-074-1255). The porous texture of the synthesized samples was investigated by N_2 adsorption measurements (Figure S4). The N_2 physisorption isotherm of NTO and CTO shows a typical type II isotherm, indicative of a non-porous solid.[48] The NTO sample presents hysteresis in the high relative pressure range due to interparticle adsorbate condensation. The latter represents a confirmation of the small size of the NTO particles, as observed by TEM analysis.[49] Table S.3 includes the textural properties, which are similar for both materials. Indeed, the two MTOs have a low BET surface area, being non-porous as shown by the N_2 physisorption isotherm. The NTO_H sample presents a greater value of S_{BET} (12.5 m^2/g) than CTO_H (7.4 m^2/g), indicating a higher surface area owing to its lower particle size, evidenced by TEM and SEM analyses (Figure 2 and Figure S.3).

The elemental distribution of the NTO and CTO samples is characterized by using energy-dispersive X-ray spectroscopy (EDS) combined with scanning TEM (STEM-EDS), as depicted in Figure 3. STEM-EDS analysis of the NTO_H (Figure 3a) and CTO_H (Figure 3b) samples shows only presence of Ni or Cu (green), Te (blue), and O (red) elements, indicating that the Na element is not incorporated in the structure of this material, as was observed in the XRD pattern. Moreover, the quantitative analysis by EDS in three different positions (Table S.4) of both samples indicates that the relative amount of the elements M (Ni or Cu), Te, and O is very close to the stochiometric ratio (M_3TeO_6).[13,50] This is another proof that the desired tellurates (M_3TeO_6) have been obtained without incorporation of Na in the structure.

The EELS spectra of the two selected nano-crystals of NTO (Figure 4a and Figure S.5a) and CTO (Figure 4b and Figure S.5b) correspond to spectroscopic signatures of O K, Te M, and Ni or Cu L edges, indicating the presence of oxygen, Te, nickel, or cooper elements. Moreover, in the NTO sample, a peak is visible in proximities of 856 and 873 eV, which may correspond to the Ni $L_{2,3}$ edge related to the presence of Ni^{2+} in the NTO sample.[39,51] The oxygen K-edge EELS spectrum of the NTO sample shows a pre-edge feature centered at ~530 eV, resulting from transitions to unoccupied 3d metal orbitals,

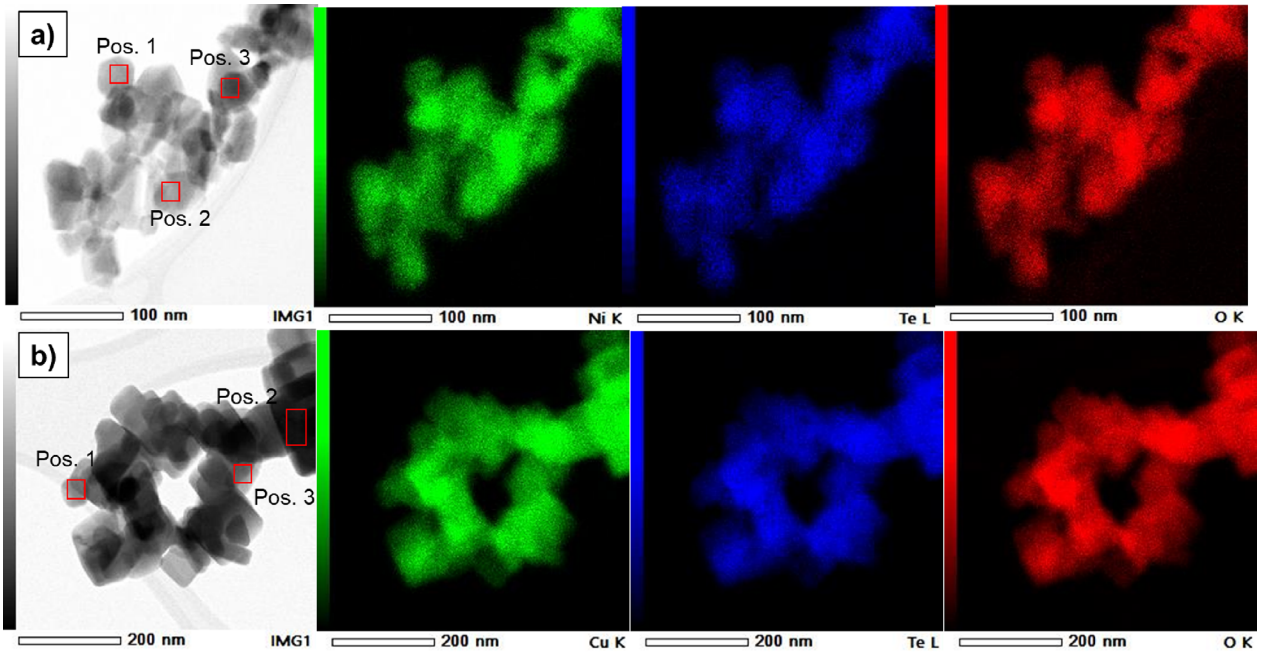

Figure 3. STEM image and corresponding EDS mapping images. (a) STEM images of NTO_H and elemental mapping images of Ni (green), Te (blue), and O (red) elements. (b) STEM images of CTO_H and elemental mapping images of Cu (green), Te (blue), and O (red) elements.

https://doi.org/10.1021/acsanm.3c00630
ACS Appl. Nano Mater. 2023, 6, 4887−4897

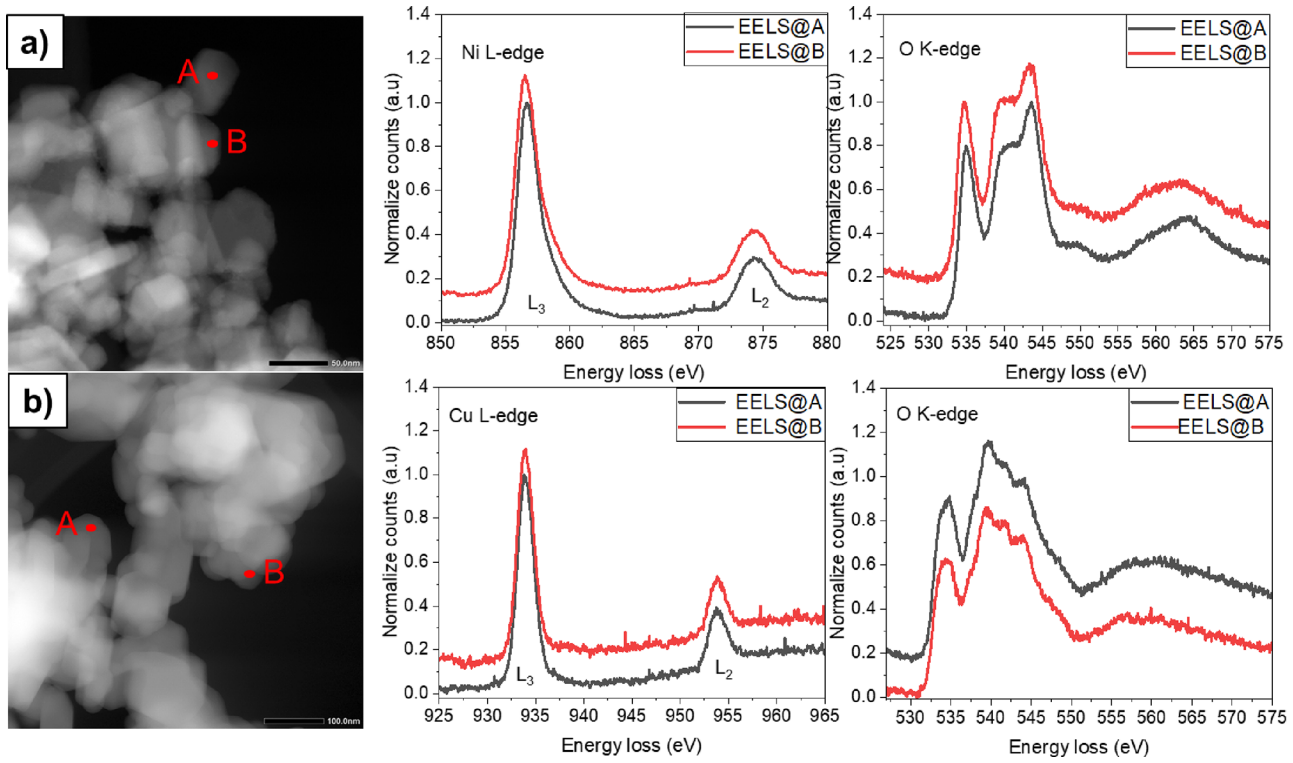

Figure 4. STEM image and corresponding EELS spectra at the marked (A and B in the image) positions for (a) NTO_H and (b) CTO_H.

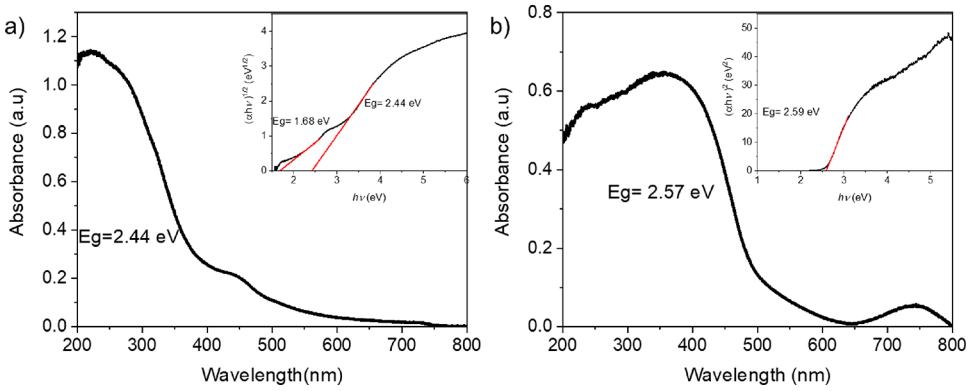

Figure 5. UV−vis spectra of (a) NTO_H and (b) CTO_H. The insets show the bandgap energy (Eg) calculation from the Tauc plot.

which are hybridized with the O 2p orbital.[39,52] In the oxygen K-edge EELS spectrum is also observed a broader band in the 535−550 eV range. The spectral intensity above the pre-edge is associated with states that have an O 2p-hybridized character with unoccupied 4s and 4p metal orbitals and Te 5pd orbitals.[53,54] The CTO_H sample shows two peaks centered in 933 and 953 eV corresponding to the Cu $L_{2,3}$ edge due to the presence of Cu^{2+}.[55] As in the NTO sample, the oxygen K-edge EELS spectrum for the CTO sample shows a pre-edge feature centered at ∼530 eV and a broader band in the 535−550 eV range, indicating the same effect. However, the pre-edge feature centered at ∼530 eV and a broader band in 535−550 eV range show some discrepancy with respect to the sample NTO, as a consequence of different bond lengths and geometrical coordination in the two samples. The latter is determined by the presence of different transition metals (Ni or Cu) and crystalline structures, as shown in the XRD pattern and widely discussed in the literature.[7,11]

To confirm the results obtained by EELS analysis, the nanomaterials synthesized by hydrothermal methodology were characterized by XPS (see Figures S6 and S7). The XPS analysis of the 2p level for the NTO_H sample (Figure S.6a) shows a peak at 855.1 eV and a satellite peak at 861.1 eV corresponding to Ni^{2+}. The XPS spectra of Ni 2p show another peak at 858.1 eV, which might indicate the presence of $Ni(OH)_2$ on the surface of the semiconductor[56] due to the use of hydrothermal synthesis, as it was previously reported for the synthesis of inorganic materials.[57] The Te 3d XPS spectra show two different peaks at 576.1 and 577.9 eV, indicating the presence of Te^{4+} and Te^{6+}. This result indicates a mixed valence of Te (Te^{4+} and Te^{6+}) in NTO materials, as it was recently reported by Numan et al.[58] The O 1s XPS spectra show a main peak at 530 eV assigned to the oxygen present in Ni_3TeO_6 lattices; another shoulder is observed at 531.3 eV, indicating the possible presence of −OH on the surface of NTO_H or oxygen vacancies to compensate the charge valence.[58] The sample CTO_H presents the divalent Cu^{2+},

https://doi.org/10.1021/acsanm.3c00630
ACS Appl. Nano Mater. 2023, 6, 4887−4897

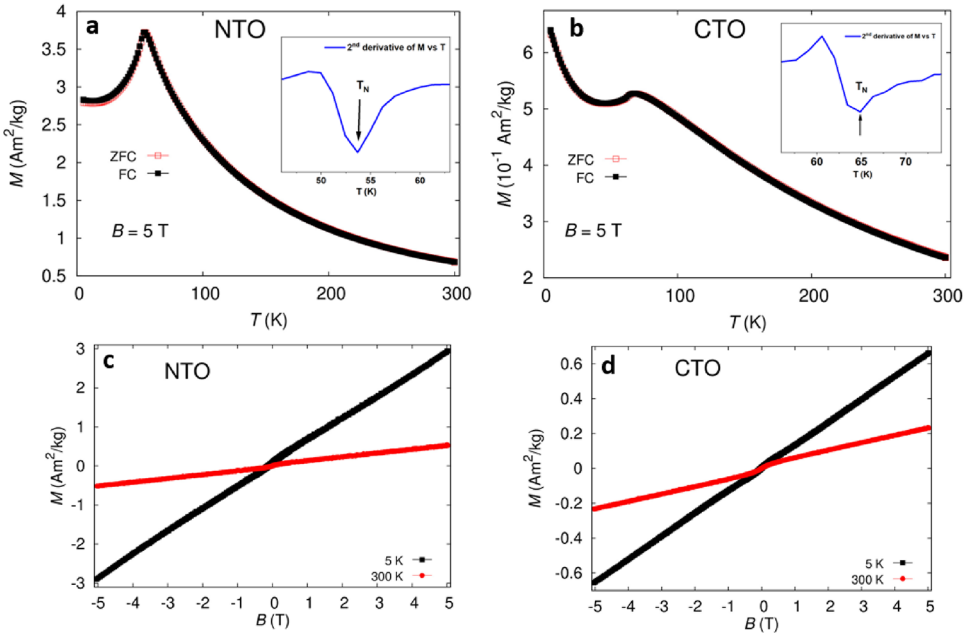

Figure 6. Magnetic domain evolution behavior studies under external field stimuli of temperature and magnetic field. (a, b) Temperature-dependent magnetization for (a) NTO and (b) CTO. (c, d) Field-dependent magnetization at 5 and 300 K for (c) NTO_H and (d) CTO_H.

since the XPS analysis of the Cu 2p level (Figure S.7a) shows a peak at 934.4 eV and a satellite peak at 940 eV.[50] The CTO_H sample also presents $Cu(OH)_2$ because Cu 2p XPS analysis shows another peak at 858.1 eV,[59] as it happens in NTO_H samples since both samples were synthesized using the same methodology. The analysis of the Te 3d XPS spectra for the CTO_H sample is difficult due to the Cu Auger peak appearing at the same range (569.2 eV). To solve this problem, the Cu Auger peak was fitted to obtain a correct background to successfully perform the analysis of Te 3d XPS peaks. The Te 3d XPS spectra show two different peaks at 576.48 and 577.3 eV, indicating the presence of Te^{4+} and Te^{6+}, as it was observed in NTO_H samples. As it was observed in NTO_H, the O 1s XPS spectra of CTO_H show a main peak at 530.46 eV assigned to the oxygen present in Cu_3TeO_6 lattices; also, the presence of a shoulder is observed at 531.3 eV indicating the possible presence of −OH on the surface of CTO_H or oxygen vacancies. The results of XPS show that the MTO NPs synthesized in this work revealed that Ni or Cu present +2 valence and Te a mixed valence in nature due to possible oxygen vacancy, as was recently reported.[58] Moreover, the MTO NPs crystallize in a single phase without incorporation of Na, as per our PXRD and EDS results.

The UV−vis spectra of NTO_H and CTO_H are shown in Figure 5. Both metal tellurates display an abrupt cutoff, as common in semiconductors.[50] The absorption spectrum of NTO_H is in the range of 200−500 nm with two main bands. The second band corresponds to the three-spin allowed d−d transition of the Ni^{2+} ions found in the structure of the material.[13,60] The CTO_H sample shows two adsorption ranges. The first one is in the range of 200−500 nm due to its semiconductor properties; meanwhile, the second absorption broad band (650−800 nm) corresponds to the d−d transitions from the Cu^{2+} ions presented in the structure of the material.[50] The bandgap (Eg) of NTO_H and CTO_H was determined by Tauc plot analysis[61] (Figure 5). The NTO_H and CTO_H samples present a band gap of 2.44 and 2.59 eV, respectively, comparable to the values present in the literature.[13,50] The Eg calculated for both metal tellurates at the nanoscale indicates that the hydrothermal methodology does not modify the optical properties of these semiconductors. Moreover, this result shows that metal tellurate nanomaterials synthesized by hydrothermal methodology possess promising optical properties and absorption in the visible range for their use in different applications.

Magnetic Properties. Figure 6a,b shows the magnetization vs temperature characteristics of NTO_H ($T_N \sim 54$ K) and CTO_H ($T_N \sim 64$ K), respectively, which are in line with the previous reports for powder as well as single-crystal enhancement of AFM interaction and transition temperature in M_3TeO_6 systems (see Table S.5).[2,4,62] The results indicate that both metal tellurates are paramagnetic (PM) in nature at room temperature. Temperature-dependent magnetization $M(T)$ measured under the field-cool (FC) and zero-field-cool (ZFC) protocol for both metal tellurates show PM behavior (Figure 6a,b). For NTO_H, the AFM coupling starts below T_N of ∼57 K (see Figure 6a). Similarly in CTO_H, magnetization increases with decreasing temperature down to 70 K and again below 25 K. The MT curve shows a drop in M at around 68 K, indicating a clear AFM coupling below this temperature. However, below 26 K, the PM phase clearly dominates, decreasing the AFM behavior at the same time (see Figure 6b). After comparing with the magnetization of single-crystal data of these two compounds, magnetization curves indicate the similar behavior of NTO_H and CTO_H with reported single crystals, showing the same intrinsic characteristics. Moreover, our NTO_H and CTO_H exhibit slightly higher AFM transition temperatures compared to those in literatures. Magnetic field dependencies at both 5 and 300 K for NTO_H and CTO_H show an increase in their magnetization with increasing external magnetic field (Figure 6c,d), being in line with the results shown in the literature.

Also, the magnetic measurement shows the ZFC and FC curves at a low magnetic field of 10 mT (Figure S.8) showing deviation from each other, due the spin-glass or cluster-glass state within the PM state. This effect is described previously by

https://doi.org/10.1021/acsanm.3c00630
ACS Appl. Nano Mater. 2023, 6, 4887−4897

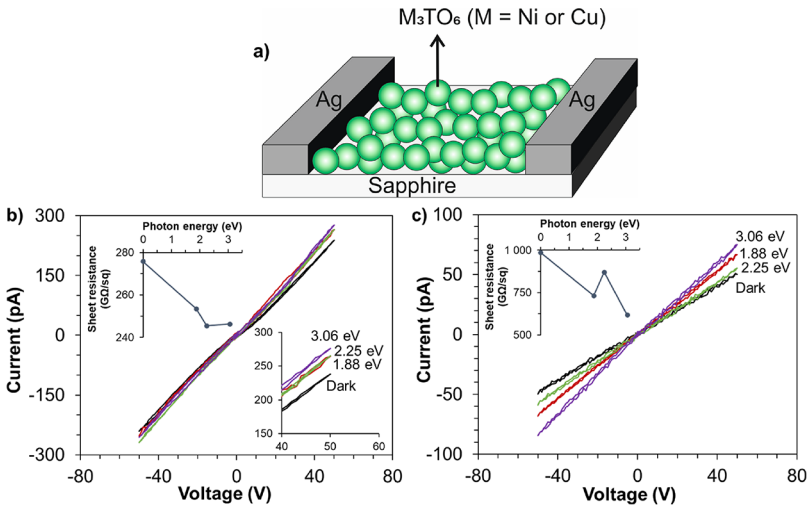

Figure 7. Photoelectrical performance of the nano-MTO-based devices. (a) Schematic of the device structure, and $I-V$ curves of (b) NTO and (c) CTO obtained under different illumination conditions. The insets of (b) and (c) show the dependence of calculated sheet resistance on incident photon energy (0 eV represents the dark).

Panneer Muthuselvam et al. for nanograin NTO, where the bulk and shell make different contributions to the superposition of the magnetic moment, as can be seen in these kinds of measurements.[62] In FC curves measured at a relatively small field, AFM coupling is relatively strong in ZFC curves, but upon FC, a clear increase in M can be seen below 57 K. Both metal tellurates present a mechanism related to the nanograined system,[62] due to the NP size of these materials, which are 37 and 140 nm for NTO_H and CTO_H, respectively (see Figure 2a,b). However, the main different behavior in magnetic properties of both metal tellurates is related in that the CTO_H sample does not have any atoms with unfilled shells, whereas NTO_H has Ni.

Photoconductivity of Metal Tellurates for Their Potential Use in Photodetection. In general, nonmetal elements with a relatively high refractive index should be photoconductive materials.[63,64] This concept has already been confirmed in terms of photoconductive effect in Te films,[65] Te nanowires,[66] and CdTe nanowires.[67] Recently, $CsCdInQ_3$ (Q = Se, Te) has also been reported to be a photoconductive compound. Although a few reports are available concerning the photo response of Te-based alloy and composition, a similar observation is missing for any of the MTO combination. To guess the photoconductive effect in MTO, we first calculated the refractive index of NTO and CTO from their measured band gaps and several established relations (see Figure S.9) and found a qualitative lead toward their possible photo response characteristics. To confirm the same, we measured the photo response of these materials.

Figure 7a illustrates the device configuration used for the $I-V$ curve measurement, which also serves as a proof-of-concept demonstration of a potential photodetection device. Figure 7b,c shows the $I-V$ curves measured on the NTO and CTO devices, respectively. Both samples exhibited photoconductivity where the sheet resistance of the NTO decreased by 14% compared with the values obtained in the dark and when exposed to violet light (3.06 eV). The response of CTO was even more obvious with a nearly 40% decrease of sheet resistance under violet light. The behavior of photoconductivity was in line with the UV−vis spectra (Figure 5) and thus confirms both NTO and CTO to be proper semiconductors with moderate band gaps. The origin of the photoconductivity observed in the NTO and CTO samples (Figure 7a,b) is due to the illumination of these semiconductors with an energy higher than the band gap (2.44 eV for NTO and 2.59 eV for CTO), which generated electron−hole pairs. This resulted in increased electrical conductivity and is the foundation of the photodetection function. Alongside the previously reported photodetection capabilities of perovskites and metal oxide semiconductors,[68−70] the test performed in this work showed that the MTO devices were able to work effectively between the green and violet light (photon energies of 2.2−3.1 eV) thanks to their moderate band gaps. This opens doors to a future violet photodetector made from the MTO nanostructures.

CONCLUSIONS

In conclusion, two metal tellurate M_3TeO_6 (M = Ni (NTO) or Cu (CTO)) at the nanoscale have been successfully synthesized via hydrothermal synthesis using NaOH as the additive. A promising hydrothermal methodology was presented, which allows the synthesis of MTOs without the incorporation of Na in the structure, resulting in the formation of $Na_2M_2TeO_6$ (NaMTO). On the contrary, the coprecipitation synthesis led to the undesired synthesis of NaMTO, as demonstrated by XRD and EDS characterization. The metal tellurates (NTO and CTO) obtained by this methodology are composed by NPs with an average size of 37 and 140 nm, respectively. NTO and CTO samples prepared in this work with NP morphology are semiconductors with band gaps of 2.44 and 2.56 eV, and both exhibited photoconductivity. In addition, NTO and CTO prepared in this work using hydrothermal synthesis present magnetic properties, with T_N of 57 and 68 K, respectively. The comparable magnetic properties and the semiconductor properties with photoconductivity of the metal tellurates synthesized by hydrothermal methodology using NaOH to the same metal tellurates prepared by a conventional approach, e.g., solid state, evidence that the use of hydrothermal methodology is an innovative methodology for the synthesis of this class of nanomaterials. This scenario opens the possibility of synthesizing new materials within this metal tellurate family using

https://doi.org/10.1021/acsanm.3c00630
ACS Appl. Nano Mater. 2023, 6, 4887−4897

hydrothermal synthesis with controlled coordination, homogeneous size crystal distribution, and different morphologies for their use in different applications. Indeed, this work serves as a preliminary proof of concept for potential application of MTO nanomaterials as photodetectors due the photoconductivity results obtained.

■ ASSOCIATED CONTENT

Supporting Information

The Supporting Information is available free of charge at https://pubs.acs.org/doi/10.1021/acsanm.3c00630.

Rietveld refinement and atomic occupancy results of SXRD data, size distribution histogram, SEM images, N_2 isotherms at 77 K and textural properties, EDS calculation of STEM-EDS images, EELS spectra for the Te M edge, and temperature-dependent magnetization (PDF)

■ AUTHOR INFORMATION

Corresponding Authors

Javier Fernández-Catalá − *Nano and Molecular Systems Research Unit, University of Oulu, Oulu FIN-90014, Finland; Materials Institute and Inorganic Chemistry Department, University of Alicante, E-03080 Alicante, Spain;* orcid.org/0000-0002-8570-2655; Email: j.fernandezcatala@ua.es

Harishchandra Singh − *Nano and Molecular Systems Research Unit, University of Oulu, Oulu FIN-90014, Finland;* orcid.org/0000-0001-7754-5648; Email: harischandra.singh@oulu.fi

Authors

Shubo Wang − *Nano and Molecular Systems Research Unit, University of Oulu, Oulu FIN-90014, Finland*

Hannu Huhtinen − *Wihuri Physical Laboratory, Department of Physics and Astronomy, University of Turku, Turku FIN-20014, Finland*

Petriina Paturi − *Wihuri Physical Laboratory, Department of Physics and Astronomy, University of Turku, Turku FIN-20014, Finland*

Yang Bai − *Microelectronics Research Unit, Faculty of Information Technology and Electrical Engineering, University of Oulu, FI-90570 Oulu, Finland;* orcid.org/0000-0002-0861-2410

Wei Cao − *Nano and Molecular Systems Research Unit, University of Oulu, Oulu FIN-90014, Finland;* orcid.org/0000-0003-3139-1780

Complete contact information is available at: https://pubs.acs.org/10.1021/acsanm.3c00630

Author Contributions

J.F.-C.: investigation, conceptualization, methodology, writing—original draft. H.S.: conceptualization, methodology, writing—review and editing. S.W.: synchrotron data acquisition and analysis, writing—review and editing. H.H. and P.P.: magnetic measurements and data analysis. Y.B.: photoconductivity measurement and interpretation. W.C.: conceptualization, review and editing, and supervision.

Notes

The authors declare no competing financial interest.

■ ACKNOWLEDGMENTS

Authors thank European Union-Next Generation EU, MINECO, and University of Alicante for a postdoctoral research grant (MARSALAS21-09), Jenny and Antti Wihuri Foundation, ERC (European Research Council) Starting Grant project UNIFY (grant agreement number 101039110), and Consolidator Grant CATCH (grant agreement no. 101002219). The authors also thank Dr. Graham King for synchrotron XRD data and the Center of Materials Analysis (CMA), University of Oulu for characterizations. Part of the research described in this work was performed at the Canadian Light Source, a national research facility of the University of Saskatchewan, which is supported by the Canada Foundation for Innovation (CFI), the Natural Sciences and Engineering Research Council (NSERC), the National Research Council (NRC), the Canadian Institutes of Health Research (CIHR), the Government of Saskatchewan, and the University of Saskatchewan.

■ REFERENCES

(1) Kim, J. W.; Artyukhin, S.; Mun, E. D.; Jaime, M.; Harrison, N.; Hansen, A.; Yang, J. J.; Oh, Y. S.; Vanderbilt, D.; Zapf, V. S.; Cheong, S. W. Successive Magnetic-Field-Induced Transitions and Colossal Magnetoelectric Effect in Ni_3TeO_6. *Phys. Rev. Lett.* **2015**, *115*, 137201.

(2) Mathieu, R.; Ivanov, S. A.; Nordblad, P.; Weil, M. Enhancement of Antiferromagnetic Interaction and Transition Temperature in M_3TeO_6 Systems (M = Mn, Co, Ni, Cu). *Eur. Phys. J. B* **2013**, *86*, 1−4.

(3) Herak, M.; Berger, H.; Prester, M.; Miljak, M.; Živković, I.; Milat, O.; Drobac, D.; Popović, S.; Zaharko, O. Novel Spin Lattice in Cu_3TeO_6: An Antiferromagnetic Order and Domain Dynamics. *J. Phys.: Condens. Matter* **2005**, *17*, 7667−7679.

(4) Oh, Y. S.; Artyukhin, S.; Yang, J. J.; Zapf, V.; Kim, J. W.; Vanderbilt, D.; Cheong, S. W. Non-Hysteretic Colossal Magnetoelectricity in a Collinear Antiferromagnet. *Nat. Commun.* **2014**, *5*, 1−7.

(5) Cheong, S. W.; Mostovoy, M. Multiferroics: A Magnetic Twist for Ferroelectricity. *Nat. Mater.* **2007**, *6*, 13−20.

(6) Zhai, K.; Shang, D.-S.; Chai, Y.-S.; Li, G.; Cai, J.-W.; Shen, B.-G.; Sun, Y. Room-Temperature Nonvolatile Memory Based on a Single-Phase Multiferroic Hexaferrite. *Adv. Funct. Mater.* **2018**, *28*, 1705771.

(7) Newnham, R. E.; Meagher, E. P. Structure of Ni_3TeO_6. *Mater. Res. Bull.* **1967**, *2*, 549−554.

(8) Yokosuk, M. O.; Al-Wahish, A.; Artyukhin, S.; O'Neal, K. R.; Mazumdar, D.; Chen, P.; Yang, J.; Oh, Y. S.; McGill, S. A.; Haule, K.; Cheong, S. W.; Vanderbilt, D.; Musfeldt, J. L. Magnetoelectric Coupling through the Spin Flop Transition in Ni_3TeO_6. *Phys. Rev. Lett.* **2016**, *117*, 1−5.

(9) Zhao, L.; Du, C. H.; Komarek, A. C. Spin-Driven Pyroelectricity in Ni_3TeO_6 without Ferroelectric Signatures of the Transition at Néel Temperature. *Phys. Status Solidi RRL* **2017**, *11*, 4−8.

(10) Yokosuk, M. O.; Artyukhin, S.; Al-Wahish, A.; Wang, X.; Yang, J.; Li, Z.; Cheong, S. W.; Vanderbilt, D.; Musfeldt, J. L. Tracking the Continuous Spin-Flop Transition in Ni_3TeO_6 by Infrared Spectroscopy. *Phys. Rev. B: Condens. Matter Mater. Phys.* **2015**, *92*, 1700073.

(11) Falck, L.; Lindqvist, O.; Moret, J. Tricopper(II) Tellurate(VI). *Acta Crystallogr.* **1978**, *18*, 896−897.

(12) Caimi, G.; Degiorgi, L.; Berger, H.; Forró, L. Optical Evidence for a Magnetically Driven Structural Transition in the Spin Web Cu_3TeO_6. *Europhys. Lett.* **2006**, *75*, 496−502.

(13) Xu, L.; Qin, C.; Xie, H.; Huang, Y.; Qin, L.; Seo, H. J. Ilmenite-Type Semiconductor Ni_3TeO_6: Preparation, Optical Property and Photo-Degradation Ability. *Mater. Lett.* **2016**, *184*, 1−4.

(14) Park, S.; Park, S.; Mathew, V.; Sambandam, B.; Hwang, J. Y.; Kim, J. A New Tellurium-Based Ni_3TeO_6-Carbon Nanotubes

Composite Anode for Na-Ion Battery. *Int. J. Energy Res.* **2022**, *46*, 16041−16049.
(15) Mutharani, B.; Rajakumaran, R.; Chen, S. M.; Ranganathan, P.; Chen, T.-W.; Al Farraj, D. A.; Ajmal, A. M.; Al-Hemaid, F. M. A. Facile Synthesis of 3D Stone-like Copper Tellurate (Cu_3TeO_6) as a New Platform for Anti-Inflammatory Drug Ibuprofen Sensor in Human Blood Serum and Urine Samples. *Microchem. J.* **2020**, *159*, 105378.
(16) Dalle, K. E.; Warnan, J.; Leung, J. J.; Reuillard, B.; Karmel, I. S.; Reisner, E. Electro- and Solar-Driven Fuel Synthesis with First Row Transition Metal Complexes. *Chem. Rev.* **2019**, *119*, 2752−2875.
(17) Zhao, X.; Shi, J.; Yin, Q.; Dong, Z.; Zhang, Y.; Kang, l.; Yu, Q.; Chen, C.; Li, J.; Liu, X.; Zhang, K. Controllable Synthesis of High-quality Two-dimensional Tellurium by a Facile Chemical Vapor Transport Strategy. *iScience.* **2022**, *25*, 103594.
(18) Rose, T. P.; Sheenu, T. Tellurium Based Materials for Nonlinear Optical Applications. *Phys. Sci. Rev.* **2022**, DOI: 10.1515/psr-2021-0117.
(19) Siritanon, T.; Laurita, G.; Macaluso, R. T.; Millican, J. M.; Sleight, A. W.; Subramanian, M. A. Observation of Electronic Conductivity in Mixed-Valence Tellurium Oxides. *Chem. Mater.* **2009**, *21*, 5572−5574.
(20) Li, J.; Siritanon, T.; Stalick, J. K.; Sleight, A. W.; Subramanian, M. A. Structural Studies and Electrical Properties of Cs/Al/Te/O Phases with the Pyrochlore Structure. *Inorg. Chem.* **2011**, *50*, 5747−5754.
(21) Sankar, R.; Shu, G. J.; Karunakara Moorthy, B.; Jayavel, R.; Chou, F. C. Growing of Fixed Orientation Plane of Single Crystal Using the Flux Growth Technique and Ferrimagnetic Ordering in Ni_3TeO_6 of Stacked 2D Honeycomb Rings. *Dalton Trans.* **2013**, *42*, 10439−10443.
(22) Zhu, X.; Wang, Z.; Su, X.; Vilarinho, P. M. New Cu_3TeO_6 Ceramics: Phase Formation and Dielectric Properties. *ACS Appl. Mater. Interfaces* **2014**, *6*, 11326−11332.
(23) Li, K.; Van Deun, R. Realizing a Novel Dazzling Far-Red-Emitting Phosphor $NaLaCaTeO_6:Mn^{4+}$ with High Quantum Yield and Luminescence Thermal Stability: Via the Ionic Couple Substitution of $Na^+ + La^{3+}$ for $2Ca^{2+}$ in $Ca_3TeO_6:Mn^{4+}$ for Indoor Plant Cultivation LEDs. *Chem. Commun.* **2019**, *55*, 10697−10700.
(24) Singh, H.; Sinha, A. K.; Gupta, S. M.; Singh, M. N.; Ghosh, H. Insight into the Growth Reaction Mechanism of Ceramic Co_3TeO_6: Synchrotron Structural and Thermal Analysis. *J. Am. Ceram. Soc.* **2016**, *99*, 3443−3448.
(25) Iqbal, M. Z.; Carleschi, E.; Doyle, B. P.; Kriek, R. J. Photocharged Water Splitting Employing a Nickel(II) Tellurium Oxide (Photo)Anode in Alkaline Medium. *ACS Appl. Energy Mater.* **2019**, *2*, 8125−8137.
(26) Dawson, W. J. Hydrothermal Synthesis of Advanced Ceramic Powders. *Am. Ceram. Soc. Bull.* **2019**, *2*, 8125−8137.
(27) Ortiz-Landeros, J.; Gómez-Yáñez, C.; López-Juárez, R.; Dávalos-Velasco, I.; Pfeiffer, H. Synthesis of Advanced Ceramics by Hydrothermal Crystallization and Modified Related Methods. *J. Adv. Ceram.* **2012**, *1*, 204−220.
(28) Shandilya, M.; Rai, R.; Singh, J. Review: Hydrothermal Technology for Smart Materials. *Adv. Appl. Ceram.* **2016**, *115*, 354−376.
(29) Chen, Y.; Li, N.; Wang, L.; Li, L.; Xu, Z.; Jiao, H.; Liu, P.; Zhu, C.; Zai, H.; Sun, M.; Zou, W.; Zhang, S.; Xing, G.; Liu, X.; Wang, J.; Li, D.; Huang, B.; Chen, Q.; Zhou, H. Impacts of Alkaline on the Defects Property and Crystallization Kinetics in Perovskite Solar Cells. *Nat. Commun.* **2019**, *10*, 1112.
(30) Somdee, A.; Osotchan, T. Effect of Precipitating Agent NaOH on the Synthesis of $SrTiO_3$ /TiO_2 Heterostructure for Dye-Sensitized Solar Cells. *Mater. Chem. Phys.* **2019**, *229*, 210−214.
(31) Liu, B.; Hu, B.; Du, Z. Hydrothermal Synthesis and Magnetic Properties of Single-Crystalline $BiFeO_3$ Nanowires. *Chem. Commun.* **2011**, *47*, 8166−8168.
(32) Sankar, R.; Panneer Muthuselvam, I.; Shu, G. J.; Chen, W. T.; Karna, S. K.; Jayavel, R.; Chou, F. C. Crystal Growth and Magnetic Ordering of $Na_2Ni_2TeO_6$ with Honeycomb Layers and $Na_2Cu_2TeO_6$ with Cu Spin Dimers. *CrystEngComm* **2014**, *16*, 10791−10796.
(33) Evstigneeva, M. A.; Nalbandyan, V. B.; Petrenko, A. A.; Medvedev, B. S.; Kataev, A. A. A New Family of Fast Sodium Ion Conductors: $Na_2M_2TeO_6$ (M = Ni, Co, Zn, Mg). *Chem. Mater.* **2011**, *23*, 1174−1181.
(34) Hausmann, J. N.; Menezes, P. W. Why should Transition Metal Chalcogenides be Investigated as Water Splitting Precatalysts even though they Transform into (oxyhydr)oxides? *Curr. Opin. Electrochem.* **2022**, *34*, 100991.
(35) Chivers, T.; Laitinen, R. S. Tellurium: a Maverick among the Chalcogens. *Chem. Soc. Rev.* **2015**, *44*, 1725−1739.
(36) Gomez, A.; Dina, G.; Kycia, S. The High-Energy x-Ray Diffraction and Scattering Beamline at the Canadian Light Source. *Rev. Sci. Instrum.* **2018**, *89*, No. 063301.
(37) Toby, B. H.; Von Dreele, R. B. GSAS-II: The Genesis of a Modern Open-Source All Purpose Crystallography Software Package. *J. Appl. Crystallogr.* **2013**, *46*, 544−549.
(38) Rietveld, H. M. A Profile Refinement Method for Nuclear and Magnetic Structures. *J. Appl. Crystallogr.* **1969**, *2*, 65−71.
(39) Patel, A. K.; Panda, M. R.; Rani, E.; Singh, H.; Samatham, S. S.; Nagendra, A.; Jha, S. N.; Bhattacharyya, D.; Suresh, K. G.; Mitra, S. Unique Structure-Induced Magnetic and Electrochemical Activity in Nanostructured Transition Metal Tellurates $Co_{1-X}Ni_XTeO_4$ (x = 0, 0.5, and 1). *ACS Appl. Energy Mater.* **2020**, *3*, 9436−9448.
(40) Dawar, R.; Babu, R.; Ananthasivan, K.; Anthonysamy, S. Thermodynamic Characterization of Ni_3TeO_6, $Ni_2Te_3O_8$ and $NiTe_2O_5$. *J. Nucl. Mater.* **2017**, *493*, 219−224.
(41) Cheng, H.; Lu, C.; Liu, J.; Yan, Y.; Han, X.; Jin, H.; Wang, Y.; Liu, Y.; Wu, C. Synchrotron Radiation X-Ray Powder Diffraction Techniques Applied in Hydrogen Storage Materials - A Review. *Prog. Nat. Sci.: Mater. Int.* **2017**, *27*, 66−73.
(42) Murtaza, T.; Kalaivanan, R.; Madeswaran, G.; Bayikadi, K.; Sankar, R. Magnetic Properties of Honeycomb Spin Lattice Compounds $Na_2M_2TeO_6$ (M = Co, Ni) and Spin Dimer Compound $Na_2Cu_2TeO_6$ Single Crystals by Flux-Growth. *J. Mater. Res. Technol.* **2021**, *14*, 1601−1608.
(43) Kadari, R.; Velchuri, R.; Reenu, K. S.; Ravi, G.; Munirathnam, N. R.; Vithal, M. Synthesis, Characterization and Tin/Copper-Nitrogen Substitutional Effect on Photocatalytic Activity of Honeycomb Ordered P_2-$Na_2Ni_2TeO_6$. *Mater. Res. Express* **2016**, *3*, 115902.
(44) Seagal, D. Chemical Synthesis of Ceramic Materials. *J. Mater. Chem.* **1997**, *7*, 1297−1305.
(45) Li, W.-N.; Yuan, J.; Shen, X.-F.; Gomez-Mower, S.; Xu, L.-P.; Sithambaram, S.; Aindow, M.; Suib, S. L. Hydrothermal Synthesis of Structure- and Shape-Controlled Manganese Oxide Octahedral Molecular Sieve Nanomaterials. *Adv. Funct. Mater.* **2006**, *16*, 1247−1253.
(46) Yan, L.; Yu, R.; Chen, J.; Xing, X. Template-Free Hydrothermal Synthesis of CeO_2 Nano-octahedrons and Nanorods: Investigation of the Morphology Evolution. *Cryst. Growth Des.* **2008**, *8*, 1474−1477.
(47) Babooram, K. *Handbook of Advanced Dielectric, Piezoelectric and Ferroelectric Materials*, 1st Edition, Woodhead: 2008, Pages 852−883
(48) Thommes, M.; Kaneko, K.; Neimark, A. V.; Olivier, J. P.; Rodriguez-Reinoso, F.; Rouquerol, J.; Sing, K. S. W. Physisorption of Gases, with Special Reference to the Evaluation of Surface Area and Pore Size Distribution. *Pure Appl. Chem.* **2015**, *87*, 1051−1069.
(49) Fernández-Catalá, J.; Cano-Casanova, L.; Lillo-Ródenas, M. Á.; Berenguer-Murcia, Á.; Cazorla-Amorós, D. Synthesis of TiO_2 with Hierarchical Porosity for the Photooxidation of Propene. *Molecules* **2017**, *22*, 2243.
(50) Mardolkar, S. D.; Salker, A. V. Insulator-Semiconductor Transitions and Photo-Luminescent Behaviour in Doped Copper Tellurates. *Mater. Sci. Semicond. Process.* **2020**, *105*, 104758.
(51) Talebi, P.; Singh, H.; Rani, E.; Huttula, M.; Cao, W. Surface Plasmon-Driven Photocatalytic Activity of Ni@NiO/$NiCO_3$ core-Shell Nanostructures. *RSC Adv.* **2021**, *11*, 2733−2743.
(52) Frati, F.; Hunault, M. O. J. Y.; de Groot, F. M. F. Oxygen K-edge X-ray Absorption Spectra. *Chem. Rev.* **2020**, *120*, 4056−4110.

(53) Sun, S.; Sun, Y.; Zhou, Y.; Xi, S.; Ren, X.; Huang, B.; Liao, H.; Wang, L. P.; Du, Y.; Xu, Z. J. Shifting Oxygen Charge Towards Octahedral Metal: A Way to Promote Water Oxidation on Cobalt Spinel Oxides. *Angew. Chem., Int. Ed.* **2019**, *131*, 6103−6108.
(54) Zhou, Y.; Sun, S.; Song, J.; Xi, S.; Chen, B.; Du, Y.; Fisher, A. C.; Cheng, F.; Wang, X.; Zhang, H.; Xu, Z. J. Enlarged Co-O Covalency in Octahedral Sites Leading to Highly Efficient Spinel Oxides for Oxygen Evolution Reaction. *Adv. Mater.* **2018**, *30*, 1802912.
(55) Laffont, L.; Wu, M. Y.; Chevallier, F.; Poizot, P.; Morcrette, M.; Tarascon, J. M. High Resolution EELS of Cu-V Oxides: Application to Batteries Materials. *Micron* **2006**, *37*, 459−464.
(56) Grosvenor, A. P.; Biesinger, M. C.; Smart, R. S. C.; McIntyre, M. S. New Interpretations of XPS Spectra of Nickel Metal and Oxides. *Surf. Sci.* **2006**, *600*, 1771−1779.
(57) Shu, Z.; Jiao, X.; Chen, D. Hydrothermal Synthesis and Selective Photocatalytic Properties of Tetragonal Star-like ZrO_2 Nanostructures. *CrystEngComm* **2013**, *15*, 4288.
(58) Numan, M.; Khan, M. S.; Majumdar, S. Vacancy Induced Mixed Valence State in Nickel Nellurate Ni_3TeO_6. *Mater. Today: Proc.* **2022**, *57*, 151−156.
(59) Vasquez, R. P. $Cu(OH)_2$ by XPS. *Surf. Sci. Spectra* **1998**, *5*, 267−272.
(60) Wang, J. L.; Li, Y. Q.; Byon, Y. J.; Mei, S. G.; Zhang, G. L. Synthesis and Characterization of $NiTiO_3$ Yellow Nano Pigment with High Solar Radiation Reflection Efficiency. *Powder Technol.* **2013**, *235*, 303−306.
(61) Makuła, P.; Pacia, M.; Macyk, W. How To Correctly Determine the Band Gap Energy of Modified Semiconductor Photocatalysts Based on UV-Vis Spectra. *J. Phys. Chem. Lett.* **2018**, *9*, 6814−6817.
(62) Panneer Muthuselvam, I.; Saranya, K.; Sankar, R.; Bhowmik, R. N.; Kavitha, L. Experimental Study of Multiple Magnetic Transitions in Micrometer and Nano-Grain Sized Ni_3TeO_6-Type Oxide. *J. Appl. Phys.* **2020**, *128*, 123902.
(63) Palik, E. D. *Handbook of Optical Constants of Solids*; 1998. Academic Press: Cambridge
(64) Bottom, V. E. The Hall Effect and Electrical Resistivity of Tellurium. *Science* **1952**, *115*, 570−571.
(65) Blackband, W. T. A Photo-Conductive Effect in Tellurium Film. *Nature* **1951**, *168*, 704.
(66) Liu, J.-W.; Zhu, J.-H.; Zhang, C.-L.; Liang, H.-W.; Yu, S.-H. Mesostructured Assemblies of Ultrathin Superlong Tellurium Nanowires and their Photoconductivity. *J. Am. Chem. Soc.* **2010**, *132*, 8945−8952.
(67) Hackney, Z.; Mair, L.; Skinner, K.; Washburn, S. Photoconductive and Polarization Properties of Individual CdTe Nanowires. *Mater. Lett.* **2010**, *64*, 2016−2018.
(68) Yang, C.; Wang, Z.; He, G.; Zhang, H.; Liao, C. $Pb_2BiS_2I_3$ Nanowires for Use in Photodetectors. *ACS Appl. Nano Mater.* **2022**, *5*, 16033−16038.
(69) White, M. A.; Dempsey, J. L.; Carroll, G. M.; Gallagher, J. D.; Gamelina, D. R. Photoconductive ZnO Films with Embedded Quantum Dot or Ruthenium Dye Sensitizers. *APL Mater.* **2013**, *1*, No. 032107.
(70) Saghaei, J.; Fallahzadeh, A.; Saghaei, T. Vapor Treatment as a New Method for Photocurrent Enhancement of UV Photodetectors Based on ZnO Nanorods. *Sens. Actuators, A* **2016**, *247*, 150−155.

https://doi.org/10.1021/acsanm.3c00630
ACS Appl. Nano Mater. 2023, 6, 4887−4897